



## Atomic structure of the Fe/Fe<sub>3</sub>C interface with the Isaichev orientation in pearlite

Y. T. Zhou, S. J. Zheng, Y. X. Jiang, T. Z. Zhao, Y. J. Wang & X. L. Ma

To cite this article: Y. T. Zhou, S. J. Zheng, Y. X. Jiang, T. Z. Zhao, Y. J. Wang & X. L. Ma (2017): Atomic structure of the Fe/Fe<sub>3</sub>C interface with the Isaichev orientation in pearlite, Philosophical Magazine, DOI: [10.1080/14786435.2017.1332434](https://doi.org/10.1080/14786435.2017.1332434)

To link to this article: <http://dx.doi.org/10.1080/14786435.2017.1332434>



Published online: 23 May 2017.



Submit your article to this journal [↗](#)



View related articles [↗](#)



View Crossmark data [↗](#)



# Atomic structure of the Fe/Fe<sub>3</sub>C interface with the Isaichev orientation in pearlite

Y. T. Zhou<sup>a</sup>, S. J. Zheng<sup>a</sup>, Y. X. Jiang<sup>a</sup>, T. Z. Zhao<sup>b</sup>, Y. J. Wang<sup>a</sup> and X. L. Ma<sup>a,c</sup>

<sup>a</sup>Shenyang National Laboratory for Materials Science, Institute of Metal Research, Chinese Academy of Sciences, Shenyang, China; <sup>b</sup>Key Laboratory of Fundamental Science for National Defence of Aeronautical Digital Manufacturing Process, Shenyang Aerospace University, Shenyang, China; <sup>c</sup>School of Materials Science and Engineering, Lanzhou University of Technology, Lanzhou, China

## ABSTRACT

The pronounced mechanical property of pearlitic steels highly correlates with the ferrite (bcc-Fe)/cementite (Fe<sub>3</sub>C) boundaries inside. Unraveling the interface structure at an atomic level is essential for interpreting the material's property. In the present study, using aberration-corrected scanning/transmission electron microscopy combined with density functional theory calculations, we reveal the atomic configuration as well as the electronic structure of the Fe/Fe<sub>3</sub>C interfaces with the Isaichev orientation in pearlite. The interface with terminating layer Fe–C–Fe in cementite has the lowest energy due to the formation of interfacial Fe–C bonds. Terrace steps which are frequently observed at the interfaces would not break the lattice match between the two phases.

## ARTICLE HISTORY

Received 17 January 2017  
Accepted 15 May 2017

## KEYWORDS

Interfaces; transmission electron microscopy; multilayers; cementite; pearlitic steel

## 1. Introduction

Nanolamellar materials have come into greater focus in the past two decades, since they possess many enhanced qualities: high strength, thermal stability, radiation damage tolerance, etc. [1–4]. Among various multilayered composites, pearlitic steel composed of ferrite/cementite lamellae should be one of the most classical engineering material, which is irreplaceably used in industry, such as rails, cables and tire cords, due to the high strength and sufficient ductility [5–8]. The extreme tensile strength of cold-drawn pearlitic steel wires even approaches 7 Gpa, making it the strongest composite in all bulk structural materials known [9].

The pronounced properties strongly correlate with the high density of interfaces inside the material. In nanostructured multilayers, the interlayer spacing cannot accommodate dislocation pile-ups and the interactions of a single dislocation with the interfaces become important [10]. The dislocation behaviours highly depend on the structural characteristics, e.g. crystallographic orientations and misfit strain

state, of the interfaces [11–13]. Particularly, the dislocation/interface interactions in pearlite would give rise to cementite decomposition by which the carbon atoms are released into ferrite and the material is further strengthened [6,14,15].

Towards fully interpreting the mechanical properties of the pearlitic steels, revealing the microstructures of the ferrite/cementite interface at an atomic level is essential, while the priority is the interfacial structures in the as-patented samples. The as-patented interface is the structural basis and the deformed structures basically come from the interactions between dislocations and the as-patented interfaces. In the past decades, considerable effort has been made to this issue. For instance, through conventional TEM, Zhou and Shiflet [16] systematically studied several crystallographic orientations and the corresponding interface structures in pearlitic steels. In a recent work, Guziewski et al. [17] performed molecular dynamics (MD) simulations to investigate the interface configurations, demonstrating that the interfaces have variant energies and misfit dislocation patterns with respect to the different terminating layers of cementite at the interface.

To our knowledge, however, the atomic configurations of the ferrite/cementite interfaces are still unclear in experiment so far. The lacking information should be attributed to the resolution deficiency of conventional TEM due to the aberrations of lens. Recent progress in aberration correction hardware in TEM makes the imaging technique a promising method for resolving the atomic configurations of interphase boundaries in alloys [18–20]. In the present work, aberration-corrected (S)TEM imaging combined with density functional theory (DFT) calculations are performed to determine the structures of the ferrite/cementite interfaces as well as the interfacial defects. The stable configuration and the binding state of the interface are unraveled. This research may provide fundamental insight into the interface-related properties in pearlitic steels.

## 2. Experimental procedure

The investigated pearlitic steel wires with a carbon content of 0.8 wt.% were supplied by Sunnywell (China) New Material Technology Co. Ltd. The as-patented samples (diameter 1.25 mm) were processed to obtain a fine pearlitic microstructure. TEM samples were prepared by standard grinding and electrochemical polishing (10% perchloric acid in ethanol). Gatan PIPS 691 ion milling was used to remove the oxide layer on sample surfaces before TEM observations.

The microstructure observations and electron diffraction analysis were performed on a FEI Tecnai G<sup>2</sup> F30 TEM. An FEI Titan Cube 60–300 TEM (operated at 300 kV) with both probe and image correctors was used to investigate the atomic-scale structures. Under scanning/transmission electron microscopy (STEM) mode, the convergent semi-angle was chosen as 20.8 mrad, and a large inner collection angle was set as 50 mrad.

### 3. DFT calculation details

All calculations were performed with Vienna *Ab initio* Simulation Package [21]. The projector-augmented wave [22,23] method was used to describe the core-valence electron interaction and the generalised gradient approximation [24] to treat the exchange correlation between electrons. The plane-wave cut-off energy was set at 400 eV and the Monkhorst-Pack scheme [25] was used for the k-point sampling. The lattice parameters of the bulk Fe<sub>3</sub>C was optimised in calculations to be  $a = 0.447$  nm,  $b = 0.502$  nm, and  $c = 0.672$  nm, which is in good agreement with experimental value of  $a = 0.452$  nm,  $b = 0.508$  nm, and  $c = 0.673$  nm [26]. The calculated result of the lattice of a bcc Fe is  $a = 0.283$  nm, close to the experimental values of  $a = 0.287$  nm [27].

Normal to the interface, a compositional stacking period in Fe<sub>3</sub>C crystal consists of three sub-layers, namely, Fe<sub>1</sub>-C-Fe<sub>2</sub> | Fe<sub>3</sub>-Fe<sub>4</sub> | Fe<sub>5</sub>-C-Fe<sub>6</sub>. Each atomic plane in the three sub-layers would possibly be the termination of Fe<sub>3</sub>C at the interface.

The lattice misfit between the two phases is very small ( $\sim 0.4\%$  in the  $[1\bar{1}0]_f/[10\bar{1}]_c$  direction and  $\sim 1\%$  in the  $[111]_f/[010]_c$  direction). Theoretically, the periodic array of misfit dislocations should be arranged with a much wide interspacing ( $\sim 50$  and  $\sim 25$  nm in the two directions, respectively, estimated by  $\lambda = b/\epsilon$ , where  $b$  is the Burgers vector projected in the direction, and  $\epsilon$  is the lattice parameter mismatch). Therefore, most of the interface areas separated by dislocations are likely to be perfectly coherency and performing the coherent interface approximation in computational simulations would be reasonable.

The coherent ferrite/cementite interface system was built by joining the ferrite part and the cementite part with slab geometry. The starting in-plane positions of the two parts were referred to the atomic-resolution STEM images and the possible configurations were tested. The initial separation between the two parts is appropriately adjusted according to the interplanar spacing of the  $(11\bar{2})$  plane in ferrite and the  $(101)$  in cementite. The ferrite part contains nine atomic sub-layers and the cementite part contains three compositional stacking periods. A vacuum layer with thickness of  $13\text{\AA}$  was inserted to separate the periodically repeated slabs. All the atoms are allowed to relax. Structures were optimised until the Hellman-Feynman forces on each atom were smaller than  $0.05\text{ eV/\AA}$ .

The interface energy of the system was calculated following the equation [28]:

$$\gamma_i = [E_{F/C} - (xE_{bulkF} + yE_{bulkC})]/A_i - (\gamma_{sF} + \gamma_{sC})$$

where  $E_{F/C}$  is the total energy of the ferrite/cementite system which contains  $x$  bulk unit cells of Fe and  $y$  unit cells of Fe<sub>3</sub>C,  $E_{bulkF}$  and  $E_{bulkC}$  are the bulk energies per formula unit in the bcc Fe and Fe<sub>3</sub>C crystal, respectively,  $A_i$  is the interface area,  $\gamma_{sF}$  and  $\gamma_{sC}$  denote the corresponding surface energies of Fe  $(11\bar{2})$  and Fe<sub>3</sub>C  $(101)$ .

## 4. Results and discussion

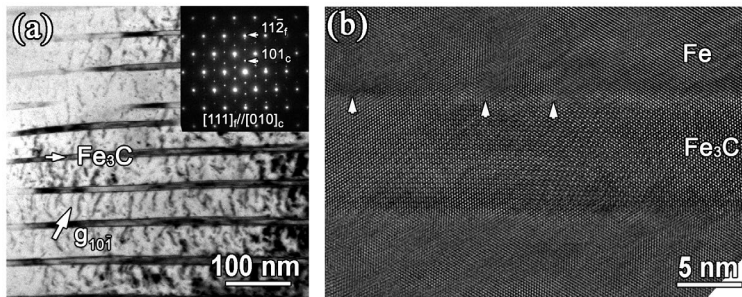
### 4.1. The structures of the ferrite/cementite interfaces in as-patented samples

Figure 1(a) shows a typical TEM image of the ferrite and cementite lamellae in a pearlite colony. Inset is the corresponding selected-area electron diffraction (SAED) pattern. Statistics show that the cementite layers parallel to each other have nearly uniform thickness which is about 10 nm, while the thickness of the ferrite layers ranges from 50 to 100 nm. The orientation relationship (OR) between ferrite and cementite is expressed as:  $[1\ 1\ 1]_f // [0\ 1\ 0]_c$ ,  $[1\ 1\ \bar{2}]_f // (1\ 0\ 1)_c$ , where the footnotes f and c refer to the ferrite phase and cementite phase, respectively. The above pearlite lamellae OR is common in the present wire, which is well known as the Isaichev relationship [16]. There are some other ORs (for instance, the Pitsch-Petch OR and the Bagaryatskii OR) in pearlite reported by previous research [16,29]. The frequency of various ORs appeared depends on the pearlite transformation temperature.

Under two-beam imaging conditions, dislocations are always clear seen in the ferrite layers and confined by the ferrite/cementite interfaces. The difference in thermal expansion coefficients between ferrite and cementite causes considerable stress and consequently the dislocations upon cooling [8].

High-resolution TEM image of the ferrite/cementite interfaces is shown in Figure 1(b). The interface exhibits a coherent and flat feature. As arrowed, the non-periodical interfacial dislocations are observed. The density of the dislocations varies from area to area. Apparently, the interspacing between dislocations in this micrograph is much smaller than the theoretical value of misfit dislocations led by lattice mismatch, but comparable with the spacing of dislocation arrays in ferrite layers. It suggests that the interfacial dislocations belong to the ‘hairpin’ dislocation loops in ferrite, as the model proposed in Ref. [10].

To resolve the atomic configuration of the ferrite/cementite interface, high-resolution HAADF STEM imaging in which the contrast intensity of an atomic



**Figure 1.** (a) A TEM micrograph of the lamellar pearlite and the corresponding selected-area electron diffraction pattern. The ferrite and cementite lamellae exhibit the Isaichev orientation relationship, i.e.  $[1\ 1\ 1]_f // [0\ 1\ 0]_c$ ,  $(1\ 1\ \bar{2})_f // (1\ 0\ 1)_c$ . (b) a high resolution TEM image of the ferrite/cementite lamellae. The interfacial dislocations are arrowed.

column is dominated by the atomic number was performed to characterise the interphase boundary. The HAADF images viewed along two perpendicular directions, i.e.  $[1\ 1\ 1]_f//[0\ 1\ 0]_c$  and  $[1\ \bar{1}\ 0]_f//[1\ 0\ \bar{1}]_c$  are, respectively, displayed in Figure 2(a) and (b). The bright dots in this image represent the positions of Fe columns. In these projections, a single column in bcc-Fe crystal contains twice Fe atoms as much as that in  $\text{Fe}_3\text{C}$  with the same thickness, therefore the ferrite shows brighter contrast. Under the imaging conditions, the  $0.75\text{\AA}$  spacing of dumbbell Fe columns is able to be resolved. Unfortunately, due to the small Z number, the carbon atoms did not show distinguishable contrast, which poses a significant hurdle to unambiguously determine the atomic configuration of the interface using HAADF imaging alone.

To address this question, first-principles calculations were applied for modelling the interfacial structures. Based on the accurate positions of Fe atoms in the HAADF images in Figure 2(a) and (b), we constructed five possible connection variants labelled as model I to V, in which the ferrite are placed atop the cementite terminated with each of the atomic planes in either the  $\text{Fe}_1\text{-C-Fe}_2$  sub-layer or the  $\text{Fe}_3\text{-Fe}_4$  sub-layer (Figure 3). The interface stability is estimated by comparing the calculated interface energies which are summarised in Table 1. The result indicates the interface with terminating plane  $\text{Fe}_1\text{-C-Fe}_2$  is most preferable.

The calculated results were verified by STEM imaging simulations on the basis of the relaxed interface structure in comparison with the experimental images. The simulation is operated by the QSTEM software [30] and takes the specimen thickness and residual lens aberrations together into account. Figure 4(a) is an enlarged experimental image of the interface viewed along the  $[1\ 1\ 1]_f//[0\ 1\ 0]_c$  direction. As a direct comparison, the simulated image is shown in Figure 4(b). The atomic positions in the relaxed slab are displayed in Figure 4(c). Because the bonding at the interface is somewhat different from that in the bulk, the atoms

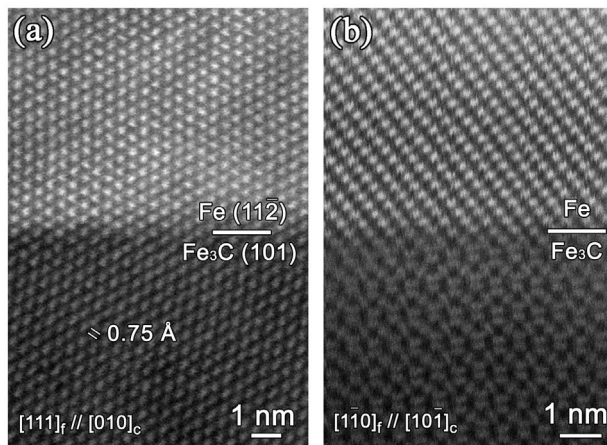


**Figure 2.** (a) High-resolution HAADF images of the ferrite/cementite interface viewed along the  $[111]_f//[010]_c$  zone axis, and (b), along the  $[1\ \bar{1}\ 0]_f//[1\ 0\ \bar{1}]_c$  zone axis, respectively.

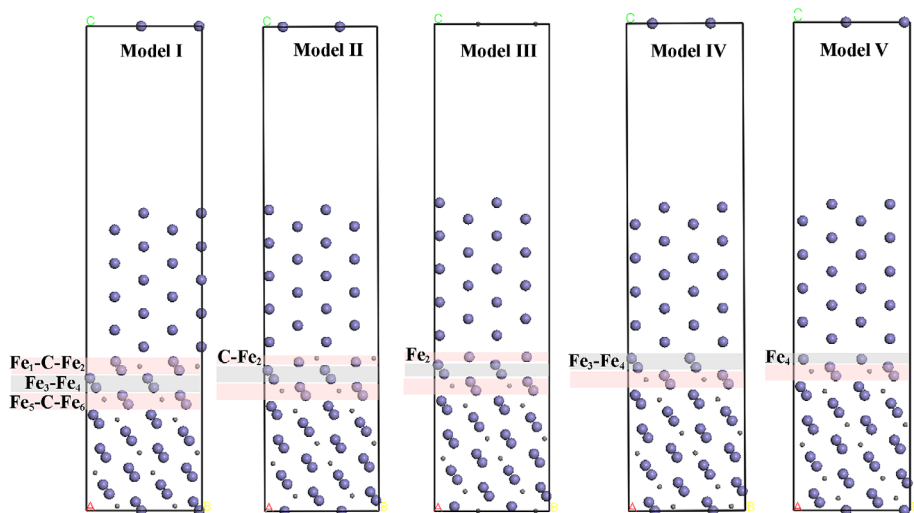


**Figure 3.** (colour online) Atomic models labelled as I–V with different terminations in cementite at the interface. The Fe–C–Fe and Fe–Fe sub-layers are highlighted by pink and grey stripes, respectively.

**Table 1.** Interface energies of the structure models labelled as I–V.

Model	I	II	III	IV	V
Energy (J/m <sup>2</sup> )	0.449	1.125	1.651	0.687	1.765

close to the interface usually rearrange their positions. Seen from the atomic positions in Figure 4(c), a slight reconstruction indeed happens in the  $\text{Fe}_1\text{-C-Fe}_2$  sub-layers in cementite near the interface. Consequently, the dumbbell Fe atoms, as denoted by arrows, get close to each other and are not able to be distinguished in both the experimental and simulated HAADF images. Nevertheless, we can still tell them apart from the Fe columns in ferrite by their dark contrast. The interfacial carbon atoms also show some deviation from the original positions (see also Figure 4(c)), which are invisible in the HAADF images. The interfacial reconstruction is more evident when it is imaged along the orthogonal direction. Figure 4(d)–(f), respectively, show the experimental micrograph, simulated image and relaxed slab model along the  $[1\bar{1}0]_f/[10\bar{1}]_c$  direction. The topmost dumbbell Fe atoms nearly superpose along the viewing direction and present as a single dot in the HAADF image. Judging from the simulated results, we can conclude that the computationally relaxed structure matches very well with the experimental findings, which further indicates the validity of the interface model.

The large difference in interface energy between the models with different interface terminations should be ascribed to the interfacial chemical environment. Figure 5(a) shows a stereoscopic illustration of the interface model I. The interfacial C atoms have the identical coordination environment with that in bulk cementite, which is enclosed by a triangular prism with six Fe atoms. The

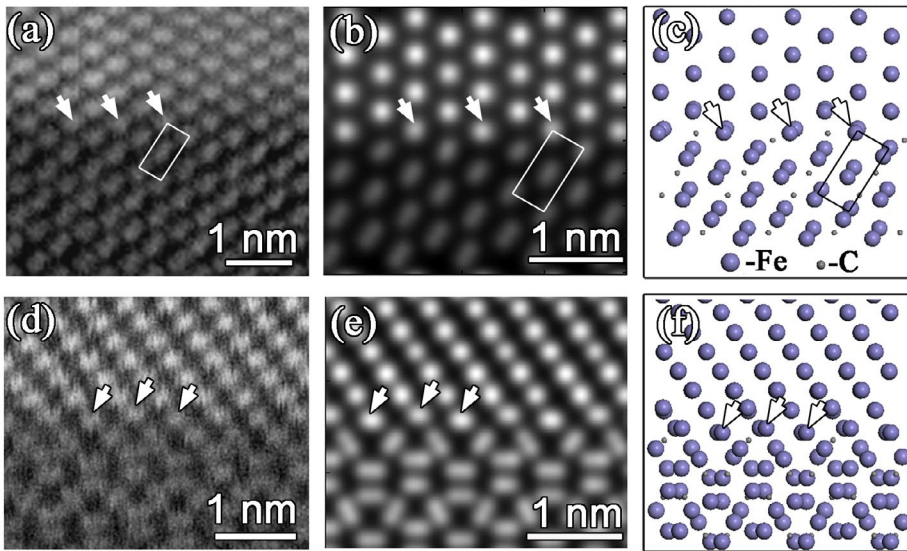


**Figure 4.** (colour online) Direct comparison between the simulated HAADF images and the experimental ones: (a) an enlarged HAADF image of the ferrite/cementite interface viewed along the  $[1\ 1\ 1]_f$  direction. (b) The simulated image based on the atomic positions shown in (c) which is the outcome of the computational relaxation. (d)–(f) are experimental HAADF image, simulated image and atomic projection, respectively, along the  $[1\ \bar{1}\ 0]_f$  direction. The arrows denote the atomic reconstruction at the interface. The HRSTEM image simulations were obtained for a specimen thickness of 15.5 nm, Cs value of  $1\ \mu\text{m}$  and a defocus value of 2 nm.

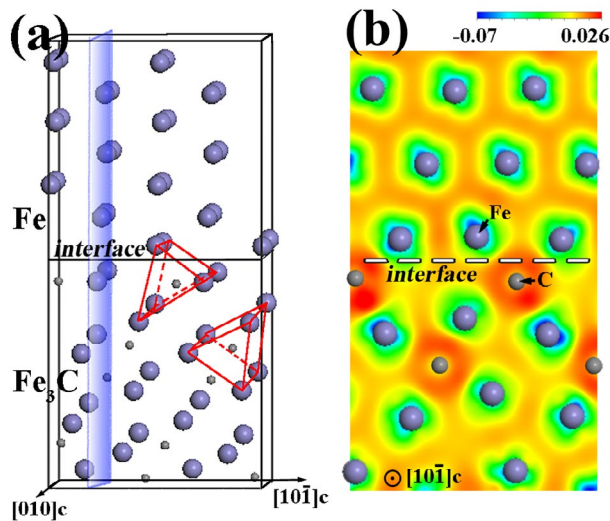


**Figure 5.** (colour online) (a) Schematic of the coordination of carbon atoms at the interface and in the bulk. (b) a slice of the differential charge density along the  $(1\ \bar{1}\ 0)_f$  plane. The position of the slice in the model is illustrated by a shadow plate in (a). The unit is  $e\text{-bohr}^{-3}$ . These pictures are produced by VESTA [33]. Electron transfer is found between the interfacial C atoms and the Fe atoms in ferrite.

Fe atoms in ferrite near the interface serve as a part of the triangular prism and form chemical bonds with the interfacial C atoms. The differential charge density is often used to illustrate naturally how the valence electrons are redistributed to form adhesive bonds. Figure 5(b) shows a  $(1\bar{1}0)_f$  slice of the differential charge density of this model. In the map, electron transfer between C and Fe atoms is clearly visible. The interfacial Fe–C bonds are very similar in character to those calculated in the bulk  $\text{Fe}_3\text{C}$ , indicating the strong bonding between cementite and ferrite layers via the interfacial C atoms.

Among these five interface slabs, model II, III, and V are non-stoichiometric. The unsaturated bonds of the interfacial carbon atoms account for the high interface energy in the three models. Regarding to model IV, the higher interface energy compared to model I should be attribute to the weak bonding between ferrite and the Fe terminating plane in cementite.

The terminating plane of cementite layer and the energy of the interface with the Bagaryatskii OR have been investigated via MD simulations by Guziewski et al. [17]. The interface with terminating FeC layer has the lowest energy, which is similar to our results. Their work suggests the energies of the interfaces with different terminations are determined by the atomic coherency and the misfit dislocation structures. Due to the computational limitations of *ab initio* method, performing calculations on a supercell that accommodates the misfit dislocation network is impractical. Thus, the effect of interfacial dislocations is neglected. Nevertheless, the lattice mismatch between ferrite and cementite with the Isaichev OR is an order of magnitude smaller than that with the Bagaryatskii OR ( $\sim 10.7\%$ ). The wide spaced misfit dislocations are believed not to have great influence on the configuration of the coherent region, although they may increase the value of the total interface energy to some extent, as suggested by Schnitker et al. [31]. It is unclear that, in the deformed pearlitic steel, whether the accumulated strain induced by the high density of dislocations at the interface (like the ones in Figure 2(b)) would change the interface configuration. This is an important question for our further study.

#### 4.2. Interfacial defects

Carefully examining the ferrite/cementite boundaries, interfacial steps are frequently seen. The interfacial steps have been investigated by Zhou et al. [16,32]. Their work demonstrated that the curvature and thickness of the cementite lamella can be adjusted by a series of steps at the interface and the true habit plane is maintained. However, due to the resolution deficiency of conventional TEM, the connection configuration of the two phases near the step could not be characterised. As an important interfacial structure, the steps are studied by high-resolution HAADF imaging in this work as well.

A typical interfacial step is displayed in Figure 6(a). The terrace is atomically flat with the habit plane  $(11\bar{2})_f/(101)_c$ . On closer inspection, the ferrite lattice

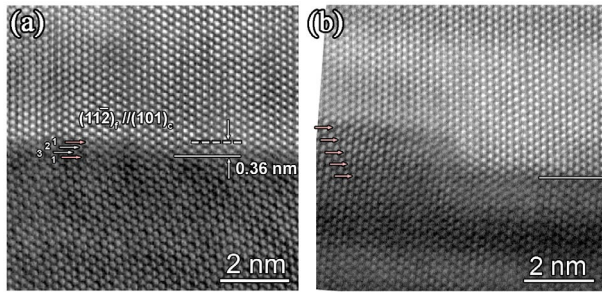


**Figure 6.** (a) A HAADF image of the terrace step at the ferrite/cementite interface. The arrows and corresponding numbers denote different (1 0 1) sub-layers in cementite. The pink arrows point to the positions of  $\text{Fe}_1\text{-C-Fe}_2$  planes. On both sides of the step, the interface keeps the stable stacking configuration as shown above. Such terrace step would not introduce any structural defects to the continuous layers. (b) An interfacial step with the height four times larger than that in (a).

matches well with cementite around the step, in other words, the step does not introduce any additive defect, such as misfit dislocation or stacking fault into the two phases. It should be attributed to that the interplanar spacing of ferrite  $(1\ \bar{1}\ \bar{2})_f$  is closely equal to the spacing between the sub-layers in cementite (1 0 1) ( $\sim 0.12$  nm). However, to maintain the afore-resolved low energy interface stacking on both sides of the step, the smallest step height is required to match the compositional stacking period, i.e. the value of three sub-layers' spacing of about 0.36 nm in cementite.

The height of the steps we observed in experiments was measured to be an integral multiple of this value. Figure 6(b) shows a terrace step whose height is four times larger than the one in Figure 6(a). The pink arrows denote the positions of the  $\text{Fe}_1\text{-C-Fe}_2$  sub-layers in cementite, which can be identified as the terminations of cementite at both the upper and lower interfaces. From the HAADF images, we can hardly define the facet of the steps. The vague contrast of the lattice fringes in cementite near the step in Figure 6(b) may indicate that the step facet inclines to the electron beam direction.

## 5. Conclusions

By means of aberration-corrected TEM and DFT calculations, the atomic-scale structures of the ferrite-cementite interfaces in pearlitic steel wires are investigated. We draw the following conclusions:

- (1) The configuration of the interface is determined as a stacking sequence of  $\text{Fe}_{\text{ferrite}}\text{-(Fe}_1\text{-C-Fe}_2\text{)}_{\text{cementite}}$ . The interfacial Fe-C bonding at the interface is the underlying reason for the stable interface configuration.
- (2) Atomic-scale imaging shows that the terrace step at the interface would not break the lattice match between ferrite and cementite. The height of

a terrace step is coincident with the compositional stacking period in cementite normal to the interface. The configuration is benefit to maintain the stable interfacial stacking on both sides of the step.

## Acknowledgement

The authors gratefully acknowledge the support of Sunnywell (China) New Material Technology Co. Ltd. for providing steel wire samples and the discussion with Mr. G. L. Zhang. We are also grateful to Mr. B. Wu and Mr. L.X. Yang at this institute for technical supports during the TEM observation. S.J.Z acknowledges the ‘Hundred Talents’ Projects of Chinese Academy of Sciences and ‘Thousand Youth Talents Plan’ of China.

## Disclosure statement

No potential conflict of interest was reported by the authors.

## Funding

This work was supported by the National Natural Science Foundation of China [grant number 51501195], [grant number 51401208], [grant number 11327901]; [grant number 51390473]; and the Fund of SYNL.

## References

- [1] I.J. Beyerlein, N.A. Mara, J.S. Carpenter, T. Nizolek, W.M. Mook, T.A. Wynn, R.J. McCabe, J.R. Mayeur, K. Kang, S. Zheng, J. Wang, and T.M. Pollock, *Interface-driven microstructure development and ultra high strength of bulk nanostructured Cu-Nb multilayers fabricated by severe plastic deformation*, *J. Mater. Res.* 28 (2013), pp. 1799–1812.
- [2] S. Zheng, I.J. Beyerlein, J.S. Carpenter, K. Kang, J. Wang, W. Han, and N.A. Mara, *High-strength and thermally stable bulk nanolayered composites due to twin-induced interfaces*, *Nat. Commun.* 4 (2013), pp. 1–8. Article ID: 1696.
- [3] M.J. Demkowicz, R.G. Hoagland, and J.P. Hirth, *Interface structure and radiation damage resistance in Cu-Nb multilayer nanocomposites*, *Phys. Rev. Lett.* 100 (2008), pp. 1–4. Article ID: 136102.
- [4] L. Lu, Y. Shen, X. Chen, L. Qian, and K. Lu, *Ultrahigh strength and high electrical conductivity in copper*, *Science* 304 (2004), pp. 422–426.
- [5] M. Zelin, *Microstructure evolution in pearlitic steels during wire drawing*, *Acta Mater.* 50 (2002), pp. 4431–4447.
- [6] X. Zhang, A. Godfrey, X. Huang, N. Hansen, and Q. Liu, *Microstructure and strengthening mechanisms in cold-drawn pearlitic steel wire*, *Acta Mater.* 59 (2011), pp. 3422–3430.
- [7] A.J. Perez-Unzueta and J.H. Beynon, *Microstructure and wear resistance of pearlitic rail steels*, *Wear* 162–164 (1993), pp. 173–182.
- [8] C. Borchers and R. Kirchheim, *Cold-drawn pearlitic steel wires*, *Prog. Mater. Sci.* 82 (2016), pp. 405–444.
- [9] Y. Li, D. Raabe, M. Herbig, P.P. Choi, S. Goto, A. Kostka, H. Yarita, C. Borchers, and R. Kirchheim, *Segregation stabilizes nanocrystalline bulk steel with near theoretical strength*, *Phys. Rev. Lett.* 113 (2014), pp. 1–4. Article ID: 106104.

- [10] A. Misra, J.P. Hirth, and H. Kung, *Single-dislocation-based strengthening mechanisms in nanoscale metallic multilayers*, *Phil. Mag.* 82 (2002), pp. 2935–2951.
- [11] R.F. Zhang, J. Wang, I.J. Beyerlein, A. Misra, and T.C. Germann, *Atomic-scale study of nucleation of dislocations from fcc–bcc interfaces*, *Acta Mater.* 60 (2012), pp. 2855–2865.
- [12] I.J. Beyerlein, J. Wang, and R. Zhang, *Interface-dependent nucleation in nanostructured layered composites*, *APL Mater.* 1 (2013), pp. 1–8. Article ID: 032112.
- [13] S.J. Zheng, J. Wang, J.S. Carpenter, W.M. Mook, P.O. Dickerson, N.A. Mara, and I.J. Beyerlein, *Plastic instability mechanisms in bimetallic nanolayered composites*, *Acta Mater.* 79 (2014), pp. 282–291.
- [14] C. Borchers, T. Al-Kassab, S. Goto, and R. Kirchheim, *Partially amorphous nanocomposite obtained from heavily deformed pearlitic steel*, *Mater. Sci. Eng. A* 502 (2009), pp. 131–138.
- [15] Y.J. Li, P. Choi, C. Borchers, S. Westerkamp, S. Goto, D. Raabe, and R. Kirchheim, *Atomic-scale mechanisms of deformation-induced cementite decomposition in pearlite*, *Acta Mater.* 59 (2011), pp. 3965–3977.
- [16] D.S. Zhou and G.J. Shiflet, *Ferrite: Cementite crystallography in pearlite*, *Metall. Trans. A* 23 (1992), pp. 1259–1269.
- [17] M. Guziowski, S.P. Coleman, and C.R. Weinberger, *Atomistic investigation into the atomic structure and energetics of the ferrite–cementite interface: The Bagaryatskii orientation*, *Acta Mater.* 119 (2016), pp. 184–192.
- [18] X.B. Hu, Y.L. Zhu, L.Z. Zhou, B. Wu, and X.L. Ma, *Atomic imaging of the interface between M23C6-type carbide and matrix in a long-term ageing polycrystalline Ni-based superalloy*, *Philos. Mag. Lett.* 95 (2015), pp. 237–244.
- [19] X.H. Shao, S.J. Zheng, D. Chen, Q.Q. Jin, Z.Z. Peng, and X.L. Ma, *Deformation twinning induced decomposition of lamellar LPSO structure and its re-precipitation in an Mg–Zn–Y alloy*, *Sci. Rep.* 6 (2016), pp. 1–9. Article ID: 30096.
- [20] S. Zheng, J.S. Carpenter, R.J. McCabe, I.J. Beyerlein, and N.A. Mara, *Engineering interface structures and thermal stabilities via SPD processing in bulk nanostructured metals*, *Sci. Rep.* 4 (2014), pp. 1–6. Article ID: 4226.
- [21] G. Kresse and J. Furthmüller, *Efficiency of ab initio total energy calculations for metals and semiconductors using a plane-wave basis set*, *Comput. Mater. Sci.* 6 (1996), pp. 15–50.
- [22] P.E. Blöchl, O. Jepsen, and O.K. Andersen, *Improved tetrahedron method for Brillouin-zone integrations*, *Phys. Rev. B* 49 (1994), pp. 16223–16233.
- [23] G. Kresse and D. Joubert, *From ultrasoft pseudopotentials to the projector augmented-wave method*, *Phys. Rev. B* 59 (1999), pp. 1758–1775.
- [24] J.P. Perdew, K. Burke, and M. Ernzerhof, *Generalized gradient approximation made simple*, *Phys. Rev. Lett.* 77 (1996), pp. 3865–3868.
- [25] H.J. Monkhorst and J.D. Pack, *Special points for Brillouin-zone integrations*, *Phys. Rev. B* 13 (1976), pp. 5188–5192.
- [26] Y.D. Zhang, J.I. Budnick, F.H. Sanchez, W.A. Hines, D.P. Yang, and J.D. Livingston, *NMR studies in orthorhombic Fe3B1–xCx (0.1 ≤ x ≤ 0.4)*, *J. Appl. Phys.* 61 (1987), pp. 4358–4360.
- [27] E.P. Yelsukov, E.V. Voronina, and V.A. Barinov, *Mössbauer study of magnetic properties formation in disordered Fe–Al alloys*, *J. Magn. Magn. Mater.* 115 (1992), pp. 271–280.
- [28] W. Liu, J.C. Li, W.T. Zheng, and Q. Jiang, *NiAl(110)/Cr(110) interface: A density functional theory study*, *Phys. Rev. B* 73 (2006), pp. 1–7. Article ID: 205421.
- [29] D. Shackleton and P. Kelly, *Orientation relationship in pearlite and the pearlite austenite interface*, *J. Iron Steel Inst.* 207 (1969), pp. 1253–1254.
- [30] C. Koch, *Determination of core structure periodicity and point defect density along dislocations* Arizona State University, 2002.
- [31] J. Schnitker and D.J. Srolovits, *Misfit effects in adhesion calculations*, *Modelling Simul. Mater. Sci. Eng.* 6 (1998), pp. 153–164.

- [32] D.S. Zhou and G.J. Shiflet, *Interfacial steps and growth mechanism in ferrous pearlites*, Metall. Trans. A 22A (1991), pp. 1349–1365.
- [33] K. Momma and F. Izumi, *VESTA: A three-dimensional visualization system for electronic and structural analysis*, J. Appl. Crystallogr. 41 (2008), pp. 653–658.